

1

2 **Supplementary Information for**

3 **Unearthing real time 3D ant tunneling mechanics**

4 **Robert Buarque de Macedo, Edward Andò, Shilpa Joy, Gioacchino Viggiani, Raj Kumar Pal, Parker, José E. Andrade**

5 **Robert Buarque de Macedo.**
6 **E-mail: rbuarque@caltech.edu**

7 **This PDF file includes:**

8 Supplementary text
9 Figs. S1 to S8 (not allowed for Brief Reports)
10 Legends for Movies S1 to S4
11 SI References

12 **Other supplementary materials for this manuscript include the following:**

13 Movies S1 to S4

14 Supporting Information Text

15 **Constructing Experimental Apparatus.** The testing apparatus was first designed and built at Caltech. This device consisted of
16 a small plastic container which could be filled with sand and ants, and placed within an XRCT scanner. The container needed
17 to be large enough such that the ants could comfortably tunnel within the domain, yet small enough to obtain detailed x-ray
18 images of all the individual grains. Furthermore, the casing needed to be cylindrical shaped so that it situated within the
19 scanner. A plastic frustum was chosen as the experimental container, which was 11.4 cm in height, 7 cm in minimum diameter
20 and 9.8 cm in maximum diameter. A plastic top for the container was 3D printed, with a hole in the center for depositing the
21 ants.

22 **Soil and Ants.** Quikrete soil of size 10/12 (1) was utilized for this experiment by passing store bought sand through a mesh size
23 10 (2 mm) followed by a mesh size 12 (1.7 mm) sieve, and keeping the grains which passed through only the former sieve.
24 Later analysis revealed the sieved granular material's average radius (maximum distance from centroid to surface) was 2.34
25 mm. Pogonomyrmex harvester ants were utilized for this experiment. Pogonomyrmex ants were chosen because of their prolific
26 digging and ability to handle grains on the mm scale, such as those used in the experiment that are ideal for XRCT imaging.
27 Ants were ordered from antsalive.com.

28 **Experimental Procedure.** The goal of the experiments was to obtain the orientations and shape of each particle in the device as
29 ants were digging. To achieve image resolution on the order of 0.1 mm, x-ray tomography was performed.

The soil sample was prepared by mixing 500 ml of 10-12 quikrete soil with 20 ml of water. This mix was poured into
31 the plastic frustum. Multiple samples were created for the experiment. The number of grains amounted to around 60,000
32 grains each time. The sample was then placed into the x-ray tomographic scanner. An initial high resolution scan with voxel
33 edge length $70\mu\text{m}$ was performed. Then, 15 ants were released at the top of the sample, and the plastic top was secured on.
34 Following this, a half-resolution scan with voxel edge length $140\mu\text{m}$ (last 4 minutes) was taken every ten minutes over the
35 course of 20 hours, thereby tracking the dynamic states of the sample. The lower resolution scans can discern particle details on
36 the scale of $\frac{1}{20}$ of the average particle diameter: enough information such that one can track the movement of all the particles
37 imaged in the initial high resolution scan. Six experiments were performed overall, however due to the XRCT machine shutting
38 off unintentionally over night, certain experiments were missing data points. Note this did not affect the quality of experiments
39 which were measured.

40 The results of these scans were 3D tiff files, each corresponding to a particular experiment and time. These tiff files were
41 then processed in the subsequent steps to obtain interparticle forces. From these images, the porosity ϕ could be determined
42 via spam (2).

43 **Image Processing.** To obtain forces between grains, we created digital particle avatars which mimicked the morphology of
44 particles in the sample. Each avatar is a 3d discrete level-set of the grain surface, along with a collection of coordinates on
45 the particle surface. For a given particle, its level set representation is a scalar function defined over three dimensional space,
46 where its value at a point is the signed distance from said point to the particle's surface, see Fig. S1. Before processing, x-ray
47 tiff images were adjusted for consistent orientation and lighting across time, and a watershed algorithm isolated the voxels
48 corresponding to each grain in the high resolution scan. This analysis was performed via the python library spam (2).

49 The process of converting a tiff file into level set particles is detailed fully in (3). In summary, non-local means filtering
50 is applied for denoising the watershed. Then, the level set of each individual grain is calculated through the process of
51 re-initialization, as are its set of surface coordinates. Particle positions and rotations are also recorded.

52 To determine the frame at which grains disappear, the lower resolution XRCT images at different instances in time, or
53 frames, were autonomously compared. For a low-resolution scan taken at a particular frame, if the mean gray value of the
54 voxels that were occupied by a particle in the initial high resolution scan dropped below 128, the grain was labeled as removed
55 and the step at which the particle disappeared was recorded.

56 **Tunnel Morphology Analysis.** To generate Fig. 2 in the text, a spline was fit to the initial positions of all particles that were
57 removed for each of the experiments. To do so, k-means clustering was first utilized to isolate the centroids of the removed
58 particles at each frame. The distances between centroids were computed to discern tunnels from one another. Then, a spline
59 was fit to each set of centroids corresponding to a particular tunnel. The spline knots could be manually perturbed for a finer
60 fit. Then, the spline was discretized into 300 points for further analysis.

61 Digging angle ϕ at a given point along the spline was determined by calculating the spline's derivative, then finding 90 –
62 the angle between this direction and the z axis. This measure was chosen because it was similar to the angle of repose for a
63 sandpile (4). For further analysis, the shape of the tunnel cross section at each spline point was calculated as follows: a plane
64 was fit at the spline point with its normal vector pointed in the direction of the spline derivative. The initial centroids of each
65 removed particle about one grain diameter away from the plane were projected onto the plane to form a 2 dimensional 'slice'.
66 Next, a convex hull was calculated from the projection of the removed particle centroids in the 2d plane. The center of the
67 convex hull was determined, and the average distance from the edge of the hull to the center was taken to be the tunnel radius
68 at this spline point. To detect which particles were on the tunnel surface at a particular frame, all grains within approximately
69 one grain diameter (2.8 mm) were classified as tunnel surface particles. Finally, principal component analysis was performed on
70 the projected centroids in the plane, and the ratio of the largest to smallest eigenvalue was taken as the tunnel aspect ratio.
71 All processing in this step was carried out by the SciPy Python library.

72 **LS-DEM Simulation.** Once the level sets and surface points of all the particles in the sample were obtained, the avatars could be
 73 used in simulation. As stated in the primary text, an extension of the DEM was used - the level set discrete element method
 74 (LS-DEM). In DEM, particles move according to classical rigid body mechanics. In the variant of interest here, particles may
 75 overlap each other. For each point on one particle which is overlapping another, a contact force is calculated. The normal force
 76 imparted from one particle onto another is a multiple of overlap distance, with constant of proportionality k_n . Shear force,
 77 perpendicular to normal force, is determined according to a Mohr-Coulomb failure criterion with coefficient of friction μ and
 78 stiffness k_s . While calculating the overlap distance is trivial for spheres, it can be difficult and computationally taxing for
 79 particles of arbitrary shape. By representing the particles as level set avatars as in LS-DEM, overlap calculations for oddly
 80 shaped particles were tractable and accurate. Wall interactions were handled through an analytical expression relating position
 81 to wall overlap. See (5) for details on LS-DEM.

82 Some particles, typically at the top and bottom of the container, were not imaged properly and their level set was non-physical.
 83 Thus, these avatars were removed before simulation. Other particles began with too high an overlap between each other,
 84 leading to high initial velocities in the simulation. This occurs usually due to errors in the image processing step. Such particles
 85 had their volume reduced by uniform contraction.

86 We use the calibration parameters similar to those in Kawamoto (6), which have been shown to predict the location and
 87 behavior of shear bands within digital twins of triaxial test. We take particle density to be 2650 kg/m^3 . k_n is the same as that
 88 in Kawamoto at ($3 * 10^4$), with a slightly reduced $k_s = 0.8k_n$. As demonstrated in (5), the specific value of k_n does not have
 89 a significant effect on results. We take $\mu = 0.45$, which is similar to but slightly lower than Kawamoto, which consisted of
 90 rougher grains. Furthermore, Kawamoto demonstrates that in the low-strain regime, such as in our sample, the response of the
 91 system to perturbation is not very sensitive to the coefficient of friction. Global damping is set to 100 s^{-1} , as it was found
 92 that this value led to efficient convergence to equilibrium, yet was large enough such that collapses and large displacements
 93 could still occur. The coefficient of restitution for local damping between grains is set to 0.4, to dampen spurious oscillations.
 94 Correctness was checked by following procedures in (7).

95 To include cohesion in the model, particle bonding was implemented according to (8). This model is equivalent to placing a
 96 beam between each pair of particles within a specified distance, which ruptures when the normal stress in the beam reaches a
 97 threshold $\sigma_c = \frac{-|F^n|}{A} + \frac{|M^s|R}{I} = \frac{C_n}{A}$ or the shear stress $\tau_c = \frac{|F^s|}{A} + \frac{|M^n|R}{J} = \frac{C_s}{A}$, where A is bond area, C_n is the maximum
 98 bond force in the normal direction and C_s is for shear, F^n and F^s are the normal and shear forces in the beam respectively,
 99 and M^n and M^s are the normal and shear moments respectively. We take the bond area $A = 1 \text{ mm}$ (referencing (9)), and I
 100 and J are the area and polar moments of inertia of the beam. The normal direction of a bond between two particles is given by
 101 the direction of the vector connecting the two closest points on the aforementioned grains. While typical liquid bond models in
 102 DEM do not provide shear or moment resistance, such models have been developed primarily for spheres (8). We find that
 103 adding shear and moment resistance is necessary for maintaining tunnel stability in all experiments. This is most likely due to
 104 the irregular shape of particles, and the more complicated geometry of cohesive bonds between grains. To validate our model,
 105 we perform angle of repose simulations along with experiments (see below). We also reproduce the DEM simulations from
 106 Santamarina et al, in which DEM particles are dropped through holes of increasing size in the flat bottom of computational
 107 silos - see figure 6 in (10). We successfully predict the regions of stability/instability in accordance with the experimental
 108 results in said paper.

109 This model was chosen as to minimize plastic contact breakage during simulation, such that the closest approximation
 110 of the force distribution in the imaged sample was obtained. The original bonding model was developed for spherical grains.
 111 Thus, we extended this formalism by calculating bond displacement from the two closest points between the participating
 112 grains at bond creation. The force needed to break bonds was calculated from equation (1) in (10):

$$113 \quad C = \frac{\pi}{2} \sigma d [2 - (\frac{8}{9} \omega G_S)^{\frac{1}{4}}] \quad [1]$$

114 with air-water surface surface tension $\sigma = 0.073 \text{ N/m}$, water content $\omega = 0.03$, specific gravity $G_S = 2.65$ and particle diameter
 115 $d = 2.3 \text{ mm}$ resulting in cohesive strength $C = 0.378 \text{ mN}$. Note this formula applies to spherical particles. We initially
 116 assumed it was a sufficient approximation for non-spherical particles due to the local smoothness of grains at contacting points.
 117 Nonetheless, it was discovered that $C_n \geq 2 * C$ for tunnels to be stable in our simulations. This may be due to the assumption
 118 of sphericity in the bond strength formula. During simulation, every 10 timesteps a particle bond is created between any
 119 unbonded pair of grains which are within 0.28 mm of each other. The normal force needed to break bonds was set to $C_n = 2C$,
 120 and shear $C_s = 0.8C_n$. Normal bond stiffness was $k_n = 2C$, and $k_s = 0.8k_n$.

121 For the first frame of the simulation, an equilibration step was conducted where particles settled from their starting
 122 configuration to a resting configuration. The simulation was run until the kinetic energy converged to a value less than
 123 $5 \text{ kg vox}^2/\text{s}^2$. We also checked that the total force on each grain was sufficiently small, such that the simulation total energy
 124 was at a stationary point.

125 The following was then performed for each frame: first, the final configuration of the previous frame was used as the initial
 126 configuration for the current. Then, the particles removed between the current and previous image were deleted from the
 127 simulation. The new configuration was run to equilibrium, and the process was then repeated for all imaged frames.

128 **Angle of Repose.** There is no agreed upon definition of the angle of repose (AOR) for a granular material, nor is there a
 129 standardized method for determining the angle - particularly for cohesive grains. For practical purposes, we define it as 'the

¹³⁰ steepest slope of the unconfined material, measured from the horizontal plane on which the material can be heaped without
¹³¹ collapsing' (4).

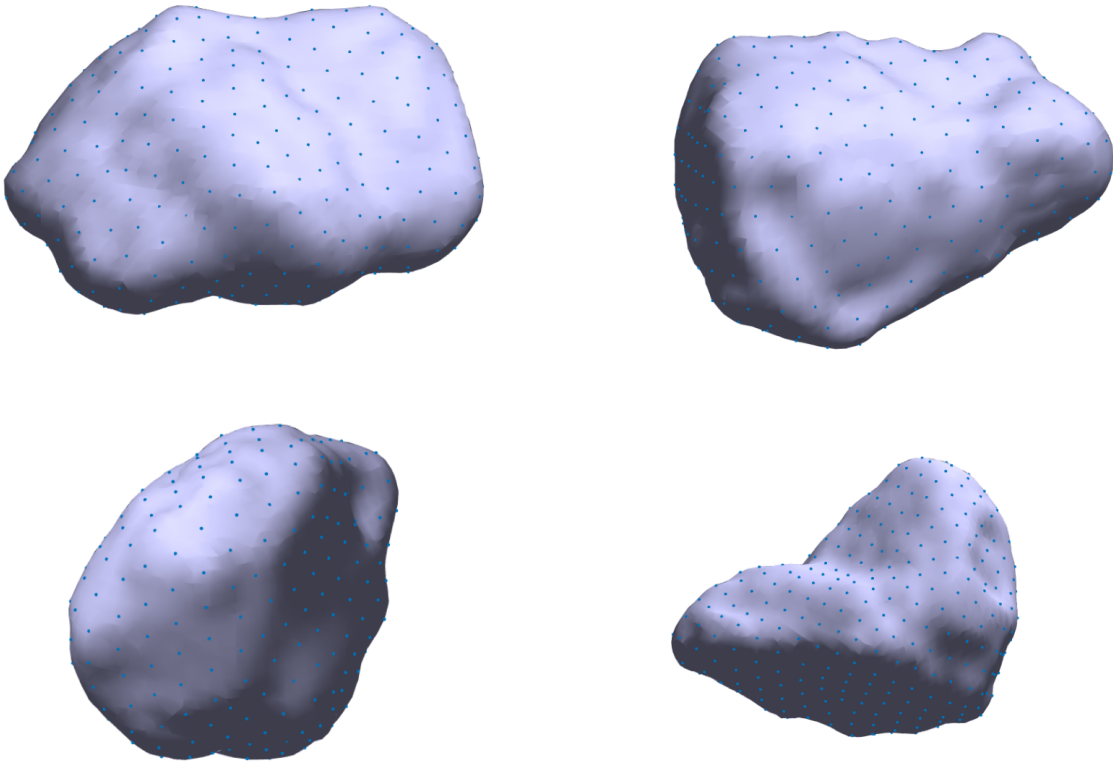


Fig. S1. Example of 4 particles used in LS-DEM simulation, obtained from XRCT. 0 isosurface of levelset given by purple mesh, with surface points superimposed.

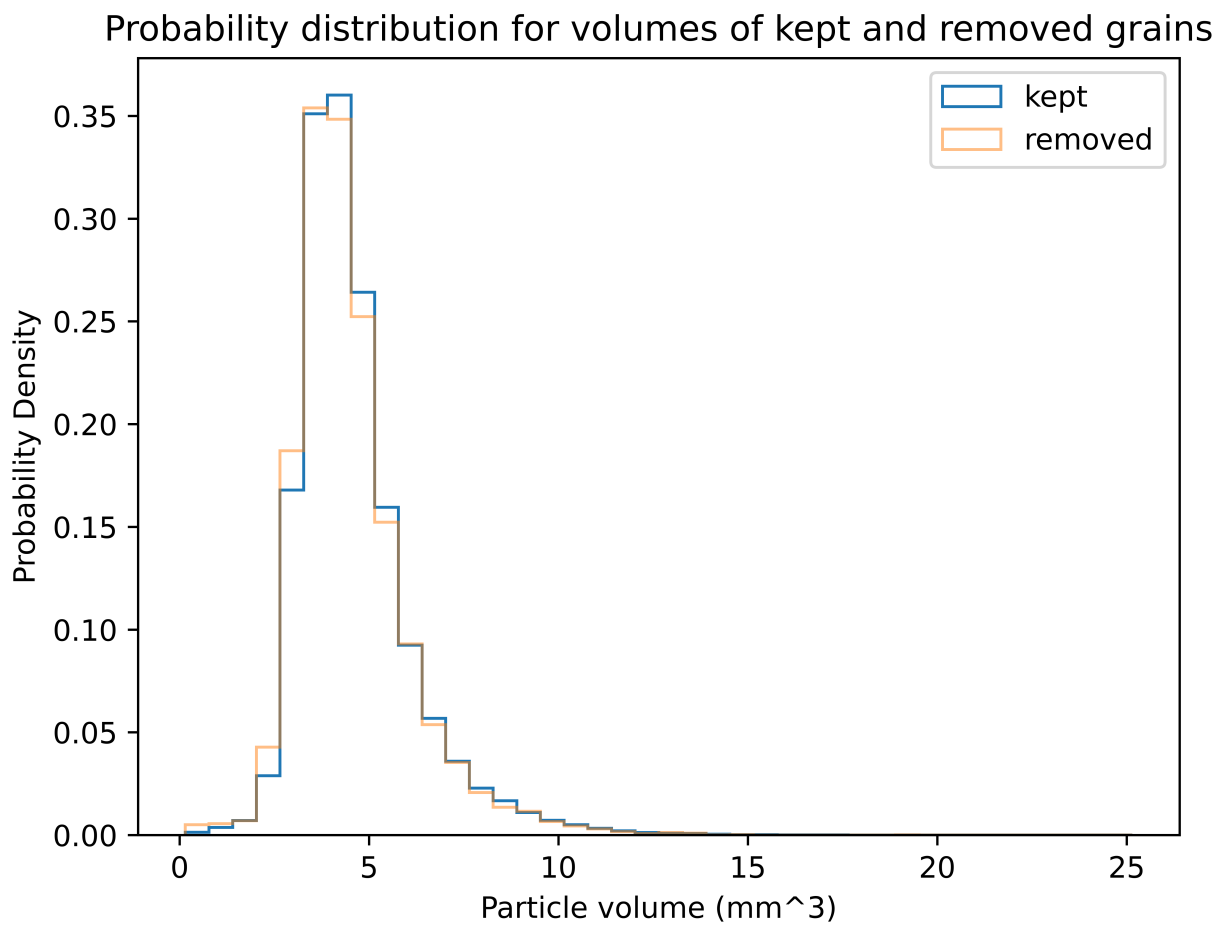


Fig. S2. Distribution of particle volumes of grains removed by ants (Removed grains) and grains kept by ants (Kept grains) across all 3 experiments. The difference between the two distributions is statistically significant, with $p \ll 0.005$ under Kolmogorov-Smirnov test.

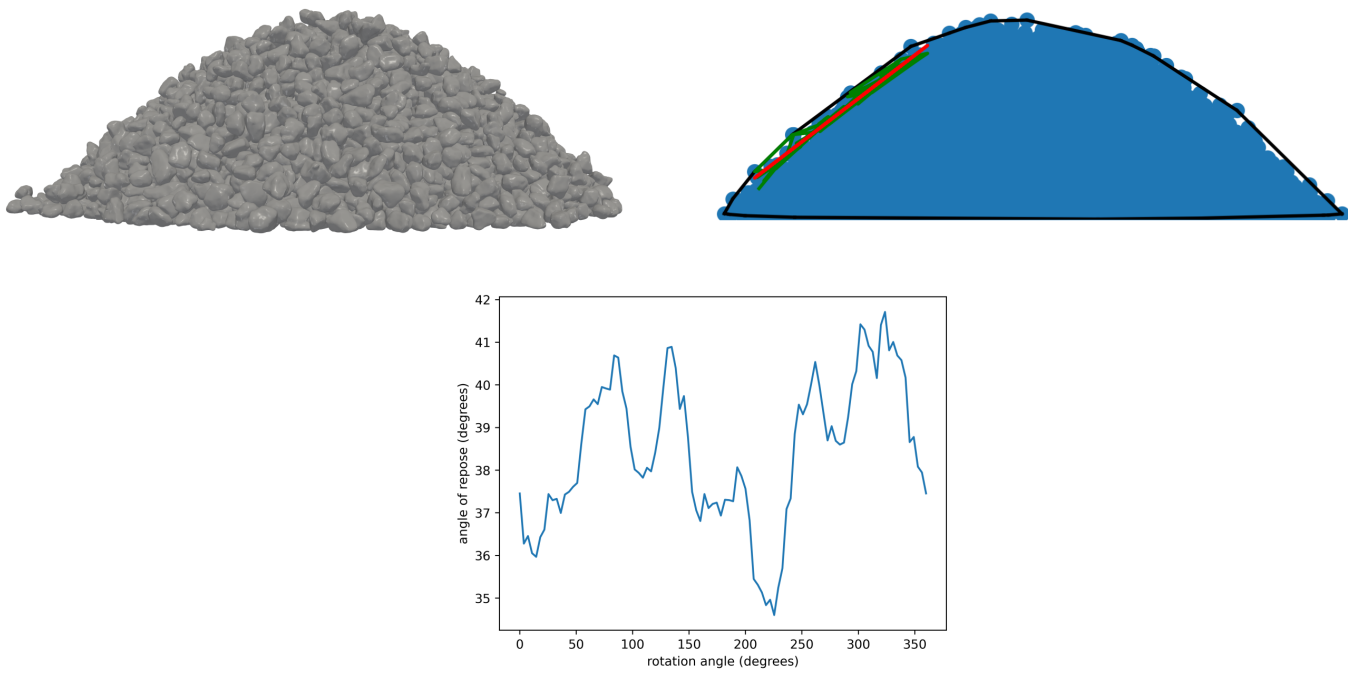


Fig. S3. LS-DEM pluviation simulation to find AOR. Particles were dropped through a filter into a conical pile (top left). Particle centroids were used to construct a 2D cross section (top right), which is centered at the origin and rotated through a circle (see movie S4). A convex hull is fit to the projection of centroids in each plane (black lines). In a given cross section, centroids used for estimating AOR were highlighted in green, with the red line denoting least squares fit. Bottom: rotation angle of projection plane vs. AOR of cross section.

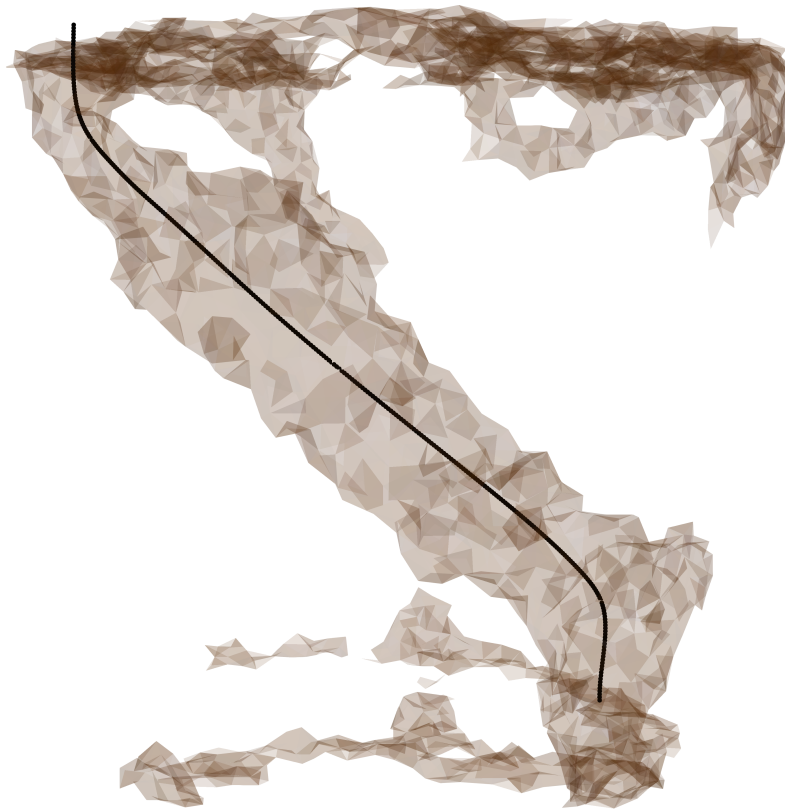


Fig. S4. Experiment 1 tunnel 1

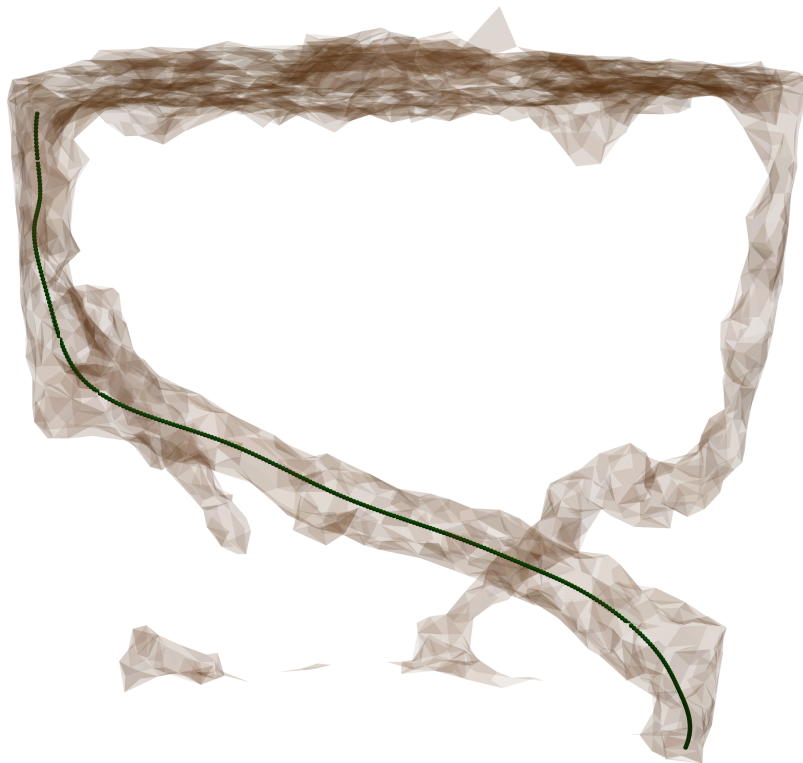


Fig. S5. Experiment 2 tunnel 1



Fig. S6. Experiment 2 tunnel 2

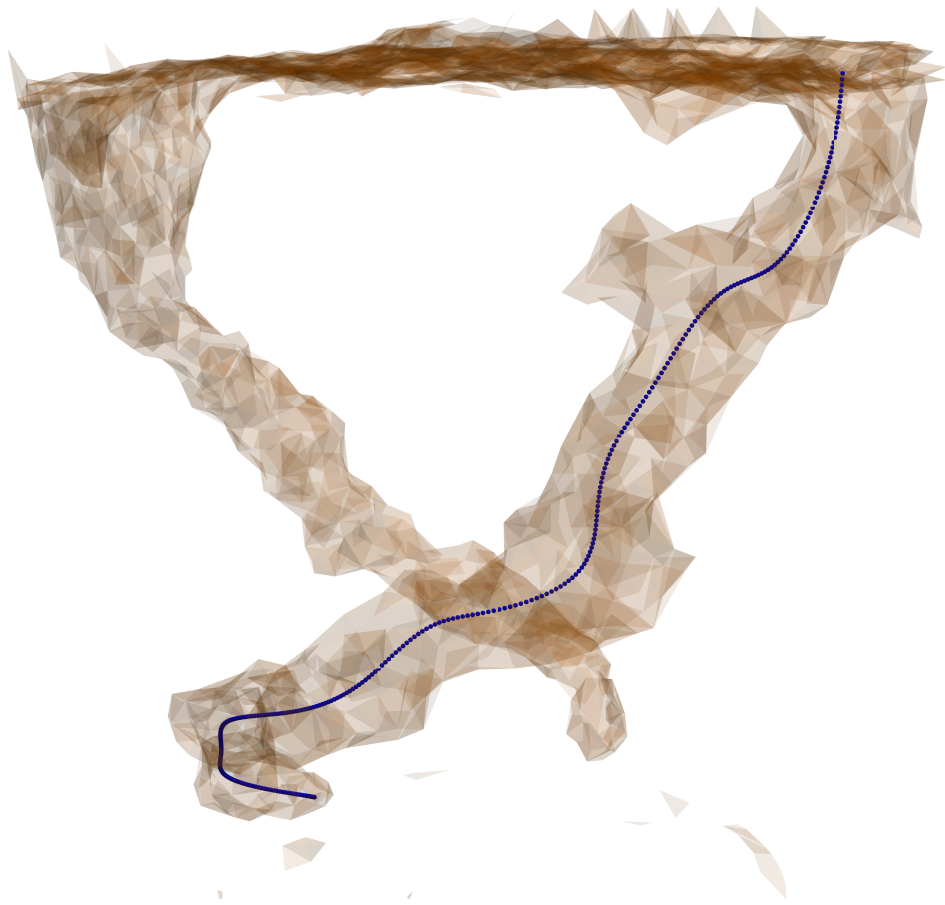


Fig. S7. Experiment 3 tunnel 1

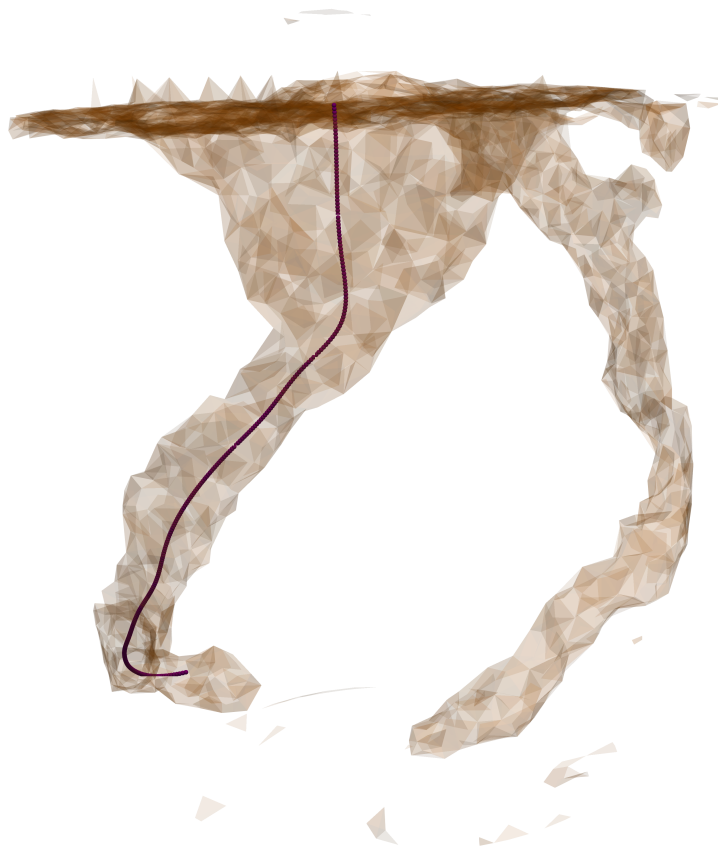


Fig. S8. Experiment 3 tunnel 2

132 Movie S1. Grains with contact forces during each stage of excavation throughout the tunnel in experiment
133 1. Each image in the video corresponds to one of the ordered points along the tunnel axis starting from
134 container top, obtained from black spline in Fig. 1. Number at the bottom indicates corresponding spline
135 point. For a given image, the cross section of the tunnel at the corresponding spline point is pictured for 8
136 x-ray scans, ordered in time chronologically. Time increases from left to right, with the top row preceding
137 the bottom row. Branch vectors are displayed, with line thickness indicating magnitude of force acting on
138 the grains involved. Yellow denotes particle that will be removed by the ants before the subsequent scan.

139 Movie S2. Video of experiment 1. On left, each image corresponds to a particular x-ray scan, or frame.
140 Digital avatars of imaged grains on the tunnel surface are rendered. Blue grains indicate particles that will
141 be removed by ants before the subsequent frame. On the right is the corresponding forces in tunnel surface
142 grains for each frame, obtained from LS-DEM simulations.

143 Movie S3. An ‘ant’s view’ of the green tunnel in experiment 2, *i.e.* what an ant would see when traversing the
144 finished tunnel. This visualization was obtained by rendering the particle avatars with the correct position
145 and rotation, as obtained from XRCT. Then, images were taken of the rendering along the interpolating
146 spline, with viewing angle given by the spline’s gradient.

147 Movie S4. Video of algorithm used to estimate angle of repose of a 3d sand pile from particle centroids.
148 Pictured is the location of particle centroids projected onto a plane with normal horizontal to gravity and
149 located at the pile center. Each frame of the video cooresponds to the plane rotated at a specific angle about
150 the z axis, see SI text and Fig. S3.

151 References

- 152 1. Mesh (scale) ([https://en.wikipedia.org/wiki/Mesh_\(scale\)](https://en.wikipedia.org/wiki/Mesh_(scale))) (2020).
- 153 2. O Stamati, et al., spam: Software for practical analysis of materials. *J. Open Source Softw.* **5**, 2286 (2020).
- 154 3. I Vlahinić, E Andò, G Viggiani, JE Andrade, Towards a more accurate characterization of granular media: extracting
155 quantitative descriptors from tomographic images. *Granul. Matter* **16**, 9–21 (2014).
- 156 4. HMB Al-Hashemi, OSB Al-Amoudi, A review on the angle of repose of granular materials. *Powder Technol.* **330**, 397–417
157 (2018).
- 158 5. R Kawamoto, E Andò, G Viggiani, JE Andrade, Level set discrete element method for three-dimensional computations
159 with triaxial case study. *J. Mech. Phys. Solids* **91**, 1 – 13 (2016).
- 160 6. R Kawamoto, E Andò, G Viggiani, JE Andrade, All you need is shape: predicting shear banding in sand with ls-dem. *J.*
161 *Mech. Phys. Solids* **111**, 375–392 (2018).
- 162 7. X Tu, JE Andrade, Criteria for static equilibrium in particulate mechanics computations. *Int. journal for numerical*
163 *methods engineering* **75**, 1581–1606 (2008).
- 164 8. DO Potyondy, P Cundall, A bonded-particle model for rock. *Int. journal rock mechanics mining sciences* **41**, 1329–1364
165 (2004).
- 166 9. V Richefeu, MS El Youssoufi, R Peyroux, F Radjai, A model of capillary cohesion for numerical simulations of 3d
167 polydisperse granular media. *Int. J. for Numer. Anal. Methods Geomech.* **32**, 1365–1383 (2008).
- 168 10. D Espinoza, J Santamarina, Ant tunneling-a granular media perspective. *Granul. Matter* **12**, 607–616 (2010).